

# Mitigating the impact of noise transients in gravitational-wave searches using reduced basis timeseries and convolutional neural networks

Ryan Magee <sup>1, a</sup>, Ritwik Sharma <sup>2</sup>, Ananya Agrawal,<sup>3</sup> and Rhiannon Udall <sup>1</sup>

<sup>1</sup>*LIGO, California Institute of Technology, Pasadena, CA 91125, USA*

<sup>2</sup>*Institut für Physik und Astronomie, Universität Potsdam,*

*Haus 28, Karl-Liebknecht-Str. 24/25, 14476, Potsdam, Germany*

<sup>3</sup>*Blue Valley West Highschool, Overland Park, KS 66085, USA*

Gravitational-wave detection pipelines have helped to identify over one hundred compact binary mergers in the data collected by the Advanced LIGO and Advanced Virgo interferometers, whose sensitivity has provided unprecedented access to the workings of the gravitational universe. The detectors are, however, subject to a wide variety of noise transients (or glitches) that can contaminate the data. Although detection pipelines utilize a variety of noise mitigation techniques, glitches can occasionally bypass these checks and produce false positives. One class of mitigation techniques is the signal consistency check, which aims to quantify how similar the observed data is to the expected signal. In this work, we describe a new signal consistency check that utilizes a set of bases that spans the gravitational-wave signal space and convolutional neural networks (CNN) to probabilistically identify glitches. We recast the basis response as a grayscale image, and train a CNN to distinguish between gravitational-waves and glitches with similar morphologies. We find that the CNN accurately classifies  $\gtrsim 99\%$  of the responses it is shown. We compare these results to a toy detection pipeline, finding that the two methods produce similar false positive rates, but that the CNN has a significantly higher true positive rate. We modify our toy model detection pipeline and demonstrate that including information from the network increases the toy pipeline's true positive rate by 4 – 7% while decreasing the false positive rate to a data-limited bound of  $\lesssim 0.1\%$ .

## I. INTRODUCTION

The Advanced LIGO [1] and Advanced Virgo [2] interferometers have provided a new way to observe our Universe. Since the detectors began observations in 2015, the LIGO-Virgo-Kagra collaboration (LVK) [3–6] and other groups [7–14] have announced the detection of gravitational waves (GWs) from over 100 unique compact binary mergers. In aggregate, these detections have shed light on the mass distribution of black holes in binaries [15], facilitated tests of general relativity [16, 17], and probed nuclear physics [18, 19]. Individually, they have challenged our understanding of stellar evolution [20–22] and yielded insight into the formation of compact binaries [23].

There are, however, a number of selection effects introduced by GW searches that can reduce our sensitivity to astrophysical sources and impact our understanding of the Universe. Excluding sources that are selected against can have a profound impact on downstream analyses [24, 25]. Some selection effects are introduced directly by the search; for example, the extent of the searched parameter space is set in advance for modeled searches. Many selection biases, however, are unknown in advance and must be mitigated against during the detection process. Most notably, this includes the impact of non-stationary noise in the detector.

Non-Gaussian noise transients, or *glitches*, pose a dual threat to detection pipelines. Glitches can contaminate

the background of the search, causing the pipeline to assign systematically lower significances to astrophysical signals [26]. Perhaps more dangerously, however, glitches can masquerade as spurious foreground signals and contaminate the purity of catalogs or low-latency GW alerts. When multiple interferometers are simultaneously collecting data, search pipelines can mandate that candidates are observed across data streams. Enforcing coincidence heavily suppresses the background; although transient noise can mimic GWs, there is a very low chance that similar deviations from Gaussianity are observed simultaneously in multiple detectors. If only one data stream is available, however, pipelines rely heavily on other quantities incorporated in their complex ranking statistics [27–29] to separate signal from noise. Unfortunately, sufficiently loud transients or those that exhibit morphologies uncharacteristic of previous data can still produce false positives.

Machine learning has recently emerged as a promising avenue towards understanding and characterizing detector noise. Machine learning-based approaches to GW astrophysics have exploded in recent years (see [30, 31] for reviews) [32–59], largely due to their ability to model complex, non-linear systems. Within GW data analysis, it promises to be especially useful in understanding the behavior of unmodeled systems, such as the transient noise present in all GW interferometers. Deep neural networks, binary classifiers, and convolutional neural networks (CNNs) have all found use in removing and classifying detector noise [60–62]. Perhaps the most well known application of machine learning to detector noise is *GravitySpy* [63, 64], which has successfully classified

---

<sup>a</sup> rmmagee@caltech.edu

thousands of glitches across a wide range of morphologies and provided reliable training data for other glitch classification and generation pipelines [65–67]. `GravitySpy` demonstrated that different classes of noise transients imprint unique signatures in the raw GW data that are identifiable by CNNs. In this work, we ask a related question: does the projection of glitches onto the compact binary coalescence (CBC) signal space elicit a unique response that can be leveraged to improve detection pipeline robustness against noise?

Here, we describe a new, machine learning-based approach to identifying and mitigating the impact of noise transients — specifically, blip glitches [68] — in detection pipelines. We focus on regions of the GW signal space that either 1) contain candidate CBCs frequently mischaracterized as noise transients [69] or 2) are representative of typical LVK detections. We recast information presently collected but discarded by the GstLAL-based inspiral pipeline [27, 70–72] as grayscale images and use CNNs [73, 74] to assign a glitch probability to GW candidates in local regions of the GW parameter space. In section II, we provide background on the search pipeline and the glitch models we use. In section III, we describe our specific application of CNNs to detection pipeline outputs. We describe the study we carry out and the training data that we generate. In section III B, we present our results and compare them to a toy model detection pipeline. We propose a modification to the toy pipeline that incorporates information from the CNN and demonstrate that it is robust against blip glitches. Finally, in IV we discuss our results and present prospects for the future.

## II. METHODS AND MOTIVATION

### A. GstLAL

Matched filter-based pipelines correlate the expected gravitational wave emission for a CBC, or *template*, with the data to calculate the complex-valued signal-to-noise ratio (SNR):

$$z_j(t) = \langle \Re(h_j(t)) | d(t) \rangle + i \langle \Im(h_j(t)) | d(t) \rangle \quad (1)$$

where  $\langle \cdot | \cdot \rangle$  denotes the noise-weighted inner product,

$$\langle a | b \rangle \equiv 4\Re \int_0^\infty df \frac{a^*(f)b(f)}{S_n(f)} \quad (2)$$

where  $h_j(t)$  is the complex-valued template and  $S_n(f)$  denotes the one-sided power spectral density (PSD). Detection pipeline compute  $\mathcal{O}(10^6)$  SNRs at a time to minimize loss of sensitivity to astrophysical transients. To reduce the cost of matched filtering, the GstLAL-based inspiral pipeline [27, 70–72] utilizes singular value decomposition (SVD) to identify orthonormal bases for local regions of the parameter space [75]. Under this formalism,

the measured SNR for template  $j$  can be written as

$$z_j(t) = \sum_{\mu} a_j^{\mu} \langle u_{\mu}(t) | d(t) \rangle \quad (3)$$

where  $a_i^{\mu}$  is the complex valued reconstruction coefficient associated with template  $j$  for basis vector  $u_{\mu}(t)$ .

In stationary, Gaussian noise, the SNR is the optimal detection statistic. Detector data, however, are neither stationary nor Gaussian, so pipelines instead rely on complex ranking statistics that incorporate a number of noise mitigation techniques. These include signal consistency checks such as  $\xi^2$ , an autocorrelation-based quantity [70] that describes a single template’s consistency in a small region of time near a candidate’s peak SNR:

$$\xi_j^2 = \frac{\int_{-\delta t}^{\delta t} dt |z_j(t) - z_j(0) R_j(t)|^2}{\int_{-\delta t}^{\delta t} dt (2 - 2|R_j(t)|^2)}. \quad (4)$$

Here,  $R_j$  represents the autocorrelation for template  $j$ , and the integrand in the denominator is a normalization term that arises from the expectation value of this quantity in Gaussian noise [70]. GstLAL records the  $\xi^2$  and  $\rho \equiv |z|$  for non-coincident<sup>1</sup>, background triggers in a histogram, and subsequently uses kernel density estimation to smooth the histogram and estimate the associated probability densities for a local group of templates  $\theta$ :  $P(\xi^2, \rho | \theta, \text{noise})$ . Glitches that cause a template to measure  $\xi^2/\rho^2 \lesssim 0.01$  are assigned a small value of  $P(\xi^2/\rho^2, \rho | \theta, \text{noise})$  and a high significance.

Here, we aim to augment our knowledge of the data surrounding a candidate by leveraging measurements made by the search across all local templates, that is, the set of raw basis responses:

$$Q_{\mu}(t) \equiv \langle u_{\mu}(t) | d(t) \rangle. \quad (5)$$

There is numerical evidence that the bases produced by SVD are complete [76] and can be interpolated to accurately reconstruct arbitrary waveforms [59, 77]. In aggregate, they span the space of CBC waveforms and may provide more information than any single template on its own. Previous work has successfully used  $Q_{\mu}(t)$  to define an alternative detection statistic for compact binary coalescences [78]. In this work, we instead use them to assign a glitch probability,  $p_{\text{glitch}}$ , to candidates in the hopes of improving the robustness of existing detection pipelines. To do this, we first recast the set of SVD SNR timeseries as grayscale images, shown in Figure 1. To help mitigate the high frequency features, we perform a Fourier Transform to express the basis responses in the frequency domain:

$$\widehat{Q}_{\mu}(f_k) = \sum_{j=0}^{N-1} Q_{\mu}(t_j) e^{-2\pi i f_k t_j} \quad (6)$$

<sup>1</sup> Background is collected only during times at which two or more interferometers of comparable sensitivity are observing.

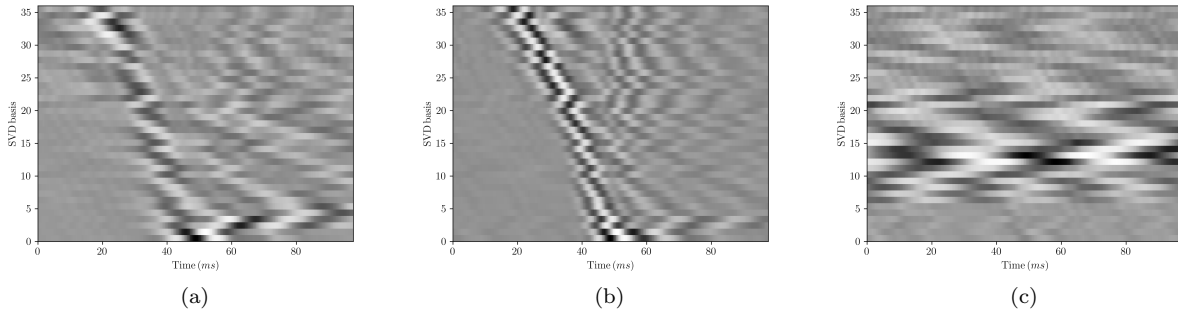


FIG. 1. The basis vector response in the time domain to a simulated GW 1a, blip glitch 1b, and scattering arch 1c. The color of each pixel corresponds to the SNR measured in that basis, at that time. Darker values correspond to higher SNRs.

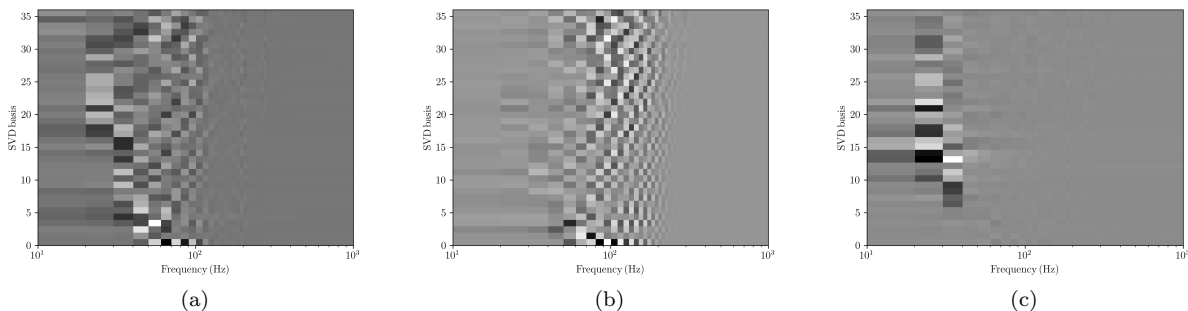


FIG. 2. The basis vector response in the frequency domain to a simulated GW 2a, blip glitch 2b, and scattering arch 2c. The color of each pixel corresponds to the SNR measured in that basis, at that frequency. Darker values correspond to higher SNRs. For compactness, we only plot the positive frequency components of the Fourier Transform.

where  $N$  is the number of data points in our original timeseries,  $t_j$  denotes a single time sample, and  $f_k$  is a single frequency point. The positive frequency components are shown in Figure 2. The full frequency domain images with positive and negative frequency components form the training data we use for the convolutional neural networks (CNNs).

## B. Glitch models

There are a wide variety of glitches that impact GW searches, but in this work we focus on blip glitches [68], which severely impact compact binary coalescence searches for sources with total mass  $M_{\text{tot}} \gtrsim 100$ , and scattered light glitches [79], which are well approximated by analytic methods and frequently overlap GW signals. Each of these transients is well modeled. Although there are several works that have presented more generic glitch models [80], they have thus far relied on using images of the time-frequency morphology to train; the models that we use are either exact or directly utilize the underlying strain data.

Blip glitches [68] are short duration  $\mathcal{O}(10\text{ms})$  transients of unknown origin that appear in both the Advanced

LIGO and Advanced Virgo interferometers. They have a similar morphology to the expected GW signature of certain types of massive black hole binaries, and they occupy the overlapping frequency band of 30 – 250 Hz. Some blips exhibit correlations with environmental conditions or subsystems at the detectors, but the vast majority lack any known correlation with monitored auxiliary channels. Although their cause remains unknown, blips are easily identifiable and cataloging efforts [63] have confidently identified thousands of them in LIGO Livingston and LIGO Hanford data. This has facilitated the development of tools, such as `gengli` [66, 67], that model this class of glitches.

`Gengli` uses generative adversarial networks (GANs) [81] to learn the underlying morphology of blip glitches, and can accurately simulate blip glitches that bear both qualitative and statistical similarity to the underlying training data. The data `gengli` uses to train is limited, however, and is heavily dependent on the GravitySpy [63] classification scheme. We assume it provides a faithful representation of blips in the remainder of this work.

While blip glitches have unknown origin, other noise transients are very well modeled by physical processes within the interferometer. *Scattered light glitches* are

a consequence of imperfections in the freely falling test masses at the LIGO detectors. Lasers incident on the mirrors can scatter away from the main beam path and rejoin after subsequent reflection off other detector components. The motion of these detector components relative to the test mass results in phase shifting of the scattered light, coupling the noise in the detector to this motion [79, 82]. This results in long duration transients that occupy the same frequency band as gravitational wave signals. Although they do not typically mimic GW signals, they were the most common glitch to overlap with true signals in O3 ( $\gtrsim 20\%$  of confident candidates) [3, 5]. We consider in particular slow scattering glitches, which result from significant motion in the microseism band [79, 83], and produce a sequence of arches due to multiple bounces from the scatterer. We approximate these arches using the model put forth in [84]. They describe the motion of the test masses as a simple harmonic oscillator, finding that the induced strain for light scattered  $N$  times is:

$$h(t) = \sum_{k=0}^N A_k \sin \left[ \frac{f_{\text{harm},k}}{f_{\text{mod}}} \sin(2\pi f_{\text{mod}}(t - t_c) + \phi_k) \right] \quad (7)$$

where  $A_k$  denotes the amplitude of the arch,  $f_{\text{harm},k}$  is the maximum frequency of the  $k$ -th harmonic,  $1/f_{\text{mod}}$  is twice the glitch duration,  $t_c$  is the glitch end time, and  $\phi_k$  is a phase offset for the  $k^{\text{th}}$  arch in the grouping.

### III. STUDY

#### A. Simulated data

We generate two BBH template banks with minimum matches [85] of 0.98 using a stochastic placement algorithm [86, 87] and a publicly available estimate of Advanced LIGO’s design sensitivity<sup>2</sup>. While constructing the banks, we model the GW emission from 20 Hz using the phenomenological waveform model IMRPhenomD [88]. The first bank is designed to recover BBHs with morphologies similar to blip glitches. We sample component masses  $10M_{\odot} < m_{1,2} < 100M_{\odot}$  and mandate total masses  $60M_{\odot} < M_{\text{tot}} < 200M_{\odot}$ . We force the component spins to be anti-aligned with the orbital angular momentum with magnitude  $|s_{1z,2z}| < 0.99$ . This results in a bank of 234 waveforms for BBHs with high total mass, asymmetric masses, and negative  $z$ -component spins. We will refer to this as the ‘glitch-like’ bank.

The second bank is designed to be representative of the population of BBHs Advanced LIGO and Advanced Virgo frequently observe, with component masses  $20M_{\odot} < m_{1,2} < 40M_{\odot}$  and negligible component spin. This simple criterion results in a bank of 53 waveforms; we will refer to this as the ‘LVK consistent’ bank in this

TABLE I. CNN Architecture for the glitch (LVK consistent) BBH banks. We use identical settings for each bank; the networks differ only due to differences in the input dimension, which is a property of the decomposed bank.

Layer Type	Kernel Size / Units	Output size
Input	37(30)x402x1	-
Conv2D	16 filters, 7x7	31(24) x 396
MaxPooling	2x2	15(12) x 198
Conv2D	32 filters, 7x7	9(6) x 192
MaxPooling	2x2	4(3) x 96
Dense	16	1

work. The banks are chosen to cover a limited parameter space to be representative of how GstLAL segments the space for filtering and background collection [89]. Studies with the glitch-like bank will demonstrate the efficacy of our method in noisy regions of the parameter space, while the LVK-consistent bank will test generality.

For each set of templates, we model the emission using the SEOBNRv4\_ROM waveform approximant [90], segment the waveforms in time [91], and perform SVD to find a set of reduced bases [75]. This results in 55 (50) bases distributed across 2 (2) time slices for the glitch-like (LVK consistent) BBH banks, respectively. For each bank, the time slice immediately prior to merger contains the majority of the signal power and is most responsive to deviations from stationarity around the coalescence. We therefore consider only this portion of the signal in the rest of this work, which results in 1 time slice of 37 (30) bases for our banks.

We likewise consider populations of both glitch-like and LVK consistent BBHs. For both sets, we generate  $10^4$  simulated signals. For the glitch-like bank, we uniformly draw component masses  $m_{1,2} \sim \mathcal{U}(10M_{\odot}, 100M_{\odot})$  and force the total mass to be  $60M_{\odot} \leq M_{\text{tot}} \leq 200M_{\odot}$ . We allow the  $z$ -component of the spin angular momentum to be either aligned or anti-aligned with the orbital angular momentum, with magnitude  $|s_{1z,2z}| \sim \mathcal{U}(0, 0.99)$ . The signals are not astrophysically distributed in space; we choose random locations, orientations, and polarizations for each system, but choose to distribute the systems uniformly in SNR,  $\rho \sim \mathcal{U}(8, 100)$ , rather than uniformly in comoving volume. For the LVK consistent BBHs, we use the same SNR distribution. These simulations, however, are non-spinning and with component masses uniformly drawn  $m_{1,2} \sim \mathcal{U}(20M_{\odot}, 40M_{\odot})$ .

We also simulate noise transients from the two well-modeled glitch classes discussed in Section II B: blip glitches and scattering arches. We use `gengli` [66, 67] to generate  $10^4$  blip glitches in the frequency band  $f \in [30\text{Hz}, 250\text{Hz}]$  with SNRs  $\rho \sim \mathcal{U}(8, 100)$ . For the scattering arches, we simulate glitches using the model described in Equation 7 from [84], fixing the number of arches to 3. Modulation frequencies are drawn uniformly over the microseism band  $f_{\text{mod}} \sim \mathcal{U}(0.05\text{ Hz}, 0.3\text{ Hz})$ . The initial arch has a peak frequency drawn from

<sup>2</sup> <https://dcc.ligo.org/LIGO-T0900288/public>

$f_{harm,0} \sim \mathcal{U}(16 \text{ Hz}, 20 \text{ Hz})$ , and the spacing between subsequent arches is drawn from a distribution  $\delta f_{harm} \sim \mathcal{U}(3 \text{ Hz}, 10 \text{ Hz})$ , such that the peak frequency of the highest arch varies from 21 Hz to 40 Hz. We once more draw  $10^4$  glitches, and rescale the amplitudes such that the SNRs are distributed between 8 and 100.

We inject the simulated BBHs and each glitch class into one month of stationary, Gaussian noise recolored to Advanced LIGO’s design sensitivity; the underlying noise is the same data used in [92]. The simulations are uniformly spaced and do not overlap in time. We also collect the response to Gaussian noise without any injected simulations. We filter each data set using both template banks described above and record the basis vector responses. We store the orthogonal SNRs observed by these bases for 0.1s centered around the time of peak injected strain. Each simulation results in a  $37 \times 201$  ( $30 \times 201$ ) matrix for the glitch-like (LVK consistent) bank. The rows, columns, and values in these matrices represent the basis vector number, time, and orthogonal SNR measured, respectively. Finally, we recast these matrices as grayscale images for input into our CNN, and use a Fourier Transform to convert to the frequency domain. We store the real and complex components in alternating columns, resulting in images with dimension  $37 \times 402$  ( $30 \times 402$ ). In total, we collect five separate sets of output per bank: the responses to glitch-like BBHs, LVK consistent BBHs, blip glitches, scattering arches, and Gaussian noise.

To facilitate comparisons to existing glitch mitigation techniques within detection pipelines, we additionally record the SNR and  $\xi^2$  value associated with the physical templates at the time of each simulated signal and glitch. Since there are multiple templates that could identify a given transient, we prefer the trigger that maximizes

$$\bar{\rho} = \frac{\rho}{\left[\frac{1}{2}(1 + \max(1, \xi^2)^3)\right]^{1/5}}, \quad (8)$$

This statistic [93, 94] is presently used in archival analyses for the same purpose.

## B. Binary classifier training and performance

For both banks, we consider four glitch scenarios and three signal scenarios. In each case, we ask if a CNN-based classifier can accurately distinguish between the glitch and signal hypothesis when presented with test data. The four glitch scenarios include the basis responses to:

- blip glitches
- scattering arches
- blip glitches and scattering arches, combined
- both glitch classes and Gaussian noise

The three signal scenarios contain the basis response to:

- high mass, high spin BBHs (glitch-like BBHs)
- nonspinning  $\sim (30M_\odot, 30M_\odot)$  BBHs (LVK consistent BBHs)
- both sets of BBHs combined

In total, we construct 12 independent binary classifiers for each bank to account for every combination of the above data. The input data,  $x_i$ , are assigned a classification,  $y_i$ , of either 0 or 1; here, we use 1 to label images containing astrophysical sources and 0 to label images that contain purely noise. We pass batches of  $N$  input images through a simple CNN consisting of two convolutional layers, each immediately followed by a pooling layer, and one fully connected layer. After each pooling layer, we use a variant of Rectified Linear Units (ReLU) known as Leaky ReLUs, as an activation function:

$$f(x) = \begin{cases} x & x > 0 \\ \alpha \cdot x & \text{else} \end{cases} \quad (9)$$

Here,  $\alpha$  is a small (non-zero) number. This modification to the standard ReLU activation function helps to mitigate against vanishing gradients throughout optimization [95]. Our output layer uses a sigmoid activation function to map our classifier to the range  $[0, 1]$ , allowing us to interpret the network output,  $y_{\text{pred},i}$ , as a probability.

We separate the data using a standard 80-10-10 split; 80% of the data is used to train the network, 10% is used to validate its performance, and 10% is reserved for testing the performance of the final model. We train using an equal amount of glitch and signal images. Noise transients, however, are much more frequent than astrophysical signals in Advanced LIGO data. Blip glitches appeared at a rate of  $\sim 50$  per day in O2 [68] and  $\sim 100$  per day in O3 [96]. By contrast, even in the current observing run, candidate GWs are only identified approximately once every 2 days<sup>3</sup>. To account for the class imbalance, we compute and minimize a weighted binary cross-entropy (BCE) loss:

$$\text{BCE loss} = -\frac{1}{N} \sum_{i=0}^N w_i y_i \ln y_{\text{pred},i} + w_i (1 - y_i) \ln(1 - y_{\text{pred},i}). \quad (10)$$

using the Adam optimizer [97]. Here, the weight  $w_i$  is a tunable parameter that sets the relative importance of each class. We apply a weight of 10 to data samples corresponding to noise transients and 1 to those of signals. This allows us to measure the performance of the network on a distribution akin to the actual data. The specific

<sup>3</sup> This is estimated from the number of significant public alerts on GraceDb.

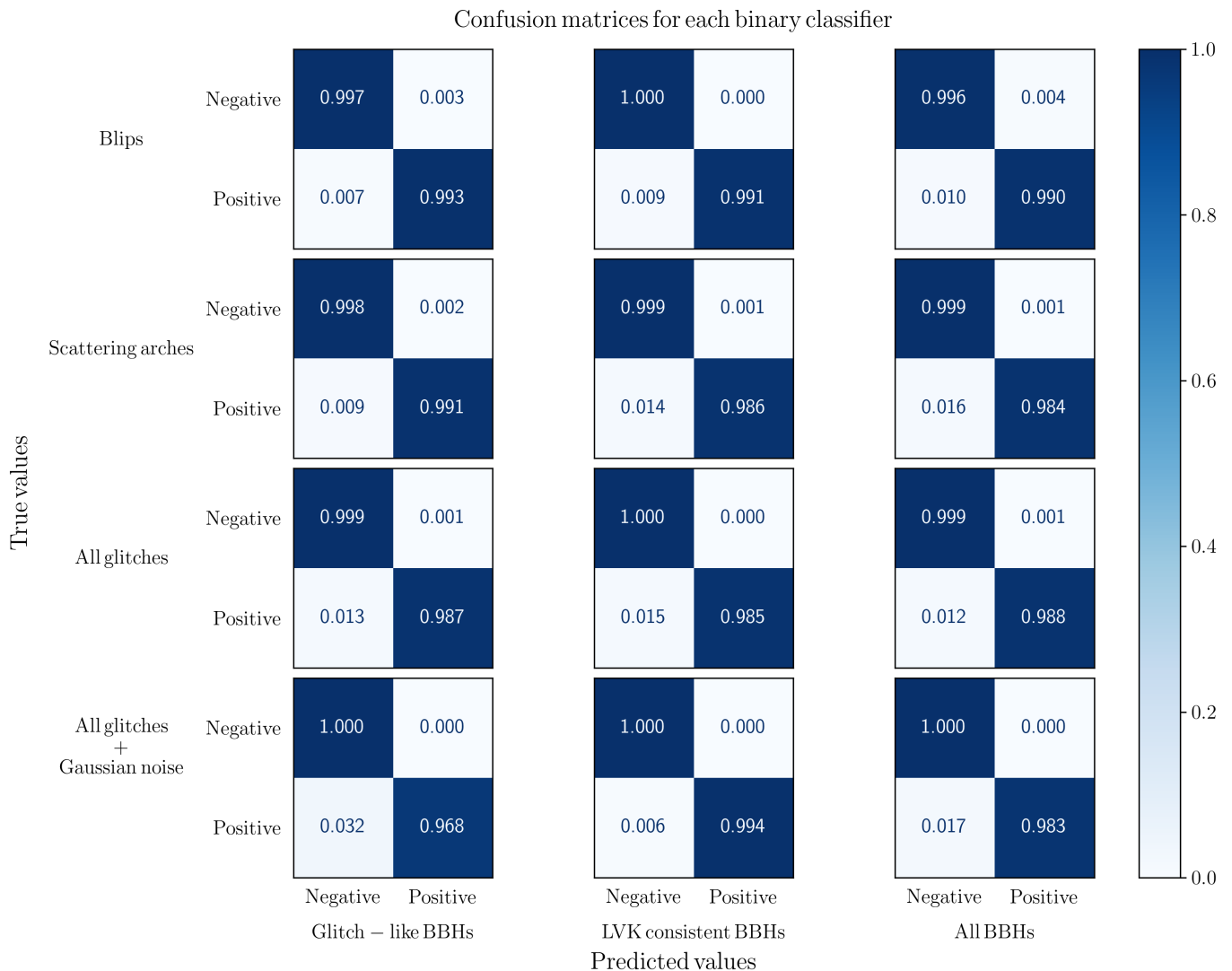


FIG. 3. Confusion matrices for each of the binary classifiers that we consider for the glitch-like BBH bank. The  $x$  and  $y$  axes for each subplot show the false and true values, respectively. The rows and columns of the entire plot show the two classes compared by the classifier. The top left corner, for example, shows the performance of the classifier in distinguishing blip glitches from a glitch-like BBH population. For this classifier, there is a true positive rate of 99% and a false positive rate of 0.7%.

architecture, kernel sizes, and output sizes for each layer of our network can be found in Table I.

The trained networks output a score that denotes the probability that a given input corresponds to a signal; we interpret this as  $p_{\text{signal}}$  and its complement,

$$p_{\text{glitch}} = 1 - p_{\text{signal}} \quad (11)$$

as the glitch probability. In order to determine if a given candidate should be classified as a signal or a glitch, we must choose a decision threshold. Naively, we might choose to label candidates with  $p_{\text{signal}} \geq 0.5$  as signals, and those with  $p_{\text{signal}} < 0.5$  as glitches. Appropriate decision thresholds, however, can vary depending on objective and performance desires. Common considerations include assessing the network’s performance on the set of

positive predictions. This includes the *precision*, or fraction of positive predictions that are actually positive, and the *recall*, or the fraction of positive predictions out of all positives in the underlying data set. Some statistics, such as the  $F_1$ -score [98], incorporate both to approximate predictive performance. Other popular measures such as the informedness [99], Matthews correlation coefficient [100], and Cohen score [101], additionally incorporate the performance of negative predictions. It is common to maximize the value of one of these fiducial statistics with respect to the decision threshold to identify the optimal threshold. In our case, we find that each classifier produces confident models, with most probabilities close to 0 or 1. This causes all of the above statistics to remain approximately constant across decision thresholds. We

therefore choose the naive boundary of 0.5.

Our results using this threshold are summarized by the confusion matrices [102] shown in Figures 3 and 4 for the glitch-like and LVK-consistent banks, respectively. In general, we find that the binary classifier consistently exhibits a high true positive rate (TPR) and low false positive rate (FPR). From the top rows, we see that blip glitches are consistently separated from GW signals; this is independent of the region of the search parameter space and the nature of the CBCs within the data. The second row in each figure considers our second fiducial glitch model, scattering arches. These have a distinct frequency evolution from GW signals (see e.g. Figures 1 and 2), so we expect that the response imprinted on the reduced bases will be distinct as well. Once again, we find that the classifiers perform well for both banks and GW signal classes. Finally, the last two rows show the performance when both glitch types are combined with each other and with Gaussian noise. Although this leads to slightly fewer true positives, the network still correctly classifies the vast majority of images.

We can interpret the first (second) *column* of Figure 3 (4) as a measure of the classifier’s discerning power when the astrophysical signal matches the confines of the bank. The second (first) *column*, on the other hand, describes the classifier’s ability to distinguish BBHs with parameters outside of its bounds from glitches. Once again, the CNN performs exceptionally, allowing us to conclude that CNNs robustly distinguish between the imprint of glitches and signals on bases that span the CBC space.

### C. Improving a toy model detection pipeline

To demonstrate how the  $p_{\text{glitch}}$  produced by our classifier can be used to improve robustness to noise transients, we construct a simple, toy model detection pipeline that incorporates both SNR and signal-consistency information and measure the performance when blip glitches are mixed with glitch-like astrophysical transients. Here, we specifically focus on the ‘glitch-like’ bank described in Section III. Following [25], we use the  $\xi^2$ -weighted SNR value  $\bar{\rho}$ , defined in Equation 8, as a ranking statistic. To provide a binary detection classification, we adopt a selection threshold of  $\bar{\rho} \geq \bar{\rho}_{\text{thresh}}$ . Signals that exceed this threshold are considered recovered by the pipeline; those below this threshold have either too low of an SNR or too poor of a  $\xi^2$  consistency check value to be deemed significant. Explicitly, we define:

$$p_{\text{signal}}(\bar{\rho}) = \begin{cases} 0 & \bar{\rho} < \bar{\rho}_{\text{thresh}} \\ 1 & \bar{\rho} \geq \bar{\rho}_{\text{thresh}} \end{cases} \quad (12)$$

We measure  $\bar{\rho}$  for each simulated signal and glitch, and impose two distinct detection thresholds ( $\bar{\rho} = 7, 10$ ) to identify marginal and confident candidates, respectively. Figure 7 shows the performance of this model. In general, we find that the toy model does an excellent job at

avoiding false positives, albeit at the cost of producing fewer true positives. At a modest threshold of  $\bar{\rho} = 7$ , we find that 92% of the simulated BBHs are correctly identified, with only 0.25% of all glitches mistakenly marked as astrophysical in origin. At the more conservative threshold of  $\bar{\rho} = 10$ , the true and false positive rates decrease to 84% and  $\lesssim 0.1\%$ , respectively. Although the FPR in each case appears low, we caution that there are  $\mathcal{O}(10^3)$  blip glitches per detector per observing run [68], and a FPR of even 0.1% would mistakenly classify several blips per observing run as astrophysical. The performance of the toy pipeline at a variety of decision thresholds is shown in Figure 5.

Thus far, we demonstrated that training on the reduced basis response produces classifiers that are at least as accurate as this toy pipeline. As a proof-of-concept demonstration for how the classifier scores might be used to mitigate the impact of glitches, we modify our original detection statistic,  $\bar{\rho}$ , to include the glitch probability as a weight on the signal consistency check:

$$\bar{\rho} = \frac{\rho}{\left[\frac{1}{2} \left(1 + \max\left(1, \frac{1}{2} p_{\text{glitch}} + 1\right) \xi^2\right)^3\right]^{1/5}}. \quad (13)$$

We choose this weighting for a few reasons. First, as in Equation 8,  $\bar{\rho} \leq \rho$ . Second, for  $p_{\text{glitch}} < 0.5$ , the network believes the data to be signal-like. In this case, the signal-consistency check is downweighted so that  $\bar{\rho}$  can increase to a maximum value of  $\rho$ . Alternatively, if  $p_{\text{glitch}} > 0.5$ , the CNN considers the data to be glitch-like and the impact of the signal consistency check is increased. Finally, if the network is uninformative at that time (e.g.  $p_{\text{glitch}} = 0.5$ ), there is no weighting applied and the ranking statistic is unchanged from the original toy pipeline. This weighting is also resistant to poorly performing classifiers; it can only increase or decrease the assigned  $\xi^2$  value by a factor of 2.

We find that applying this weight within the toy pipeline increases the TPR and the decreases the FPR across detection thresholds. This performance is summarized at a variety of decision thresholds in Figure 6. In particular, we note that at the two thresholds previously considered ( $\bar{\rho} = 7, 10$ ) the TPR increases from 94% to 98% and 84% to 90%, respectively. The FPR also improves, dropping from 1% to  $\lesssim 0.1\%$  for  $\bar{\rho} = 7$  (and remaining below our lower bound of  $\lesssim 0.1\%$  for  $\bar{\rho} = 10$ ).

## IV. DISCUSSION

Noise transients in Advanced LIGO and Advanced Virgo data can mimic high-mass BBHs, which remain a target for GW searches despite the expected dearth of black holes between  $\sim 45M_{\odot}$  and  $\sim 120M_{\odot}$  from pair-instability supernovae [103–106]. The detection of a system with component masses in the above range would bolster existing observations [21, 107] and help better constrain binary formation channels. The continued development of noise mitigation techniques and signal con-



FIG. 4. Confusion matrices for each of the binary classifiers that we consider for the LVK consistent BBH bank. The  $x$  and  $y$  axes for each subplot show the false and true values, respectively.

sistency checks for detection pipelines is therefore crucial to increase the purity of our GW catalogs, and help us to more robustly identify populations of interest.

In this work, we have demonstrated that a CNN trained to distinguish between the projection of glitches and signals on a set of reduced bases has a true positive rate of  $\gtrsim 99\%$  across a variety of scenarios. On its own, this method rejects a similar number of candidates as the toy detection pipeline we consider. It does, however, reject complementary candidates and exhibit a higher TPR and lower FPR than the unaltered pipeline. We show that incorporating the glitch probability estimated by the classifier into our toy detection pipeline increases its sensitivity across detection thresholds, suggesting that this method may be worth integrating more rigorously in production pipelines.

This study reveals a number of key findings. First, it reinforces that modern detection pipelines excel at ig-

norning noise transients. Although blip glitches and other noise transients can appear significant during single interferometer times, even the simple detection pipeline we considered rejected the vast majority of transients.

Second, we find that CNNs generically separate signals from noise transients. Since modern search pipelines [27] partition the GW parameter space, we considered two distinct regions of the BBH space. Although each classifier was trained on noise transients and the specific class of BBHs within the confines of that bank, they still successfully identified GWs from other BBH regions as signals. This remained true as we expanded the number of transient classes included in our signal and noise training sets.

Third, when the responses to multiple glitch classes are combined with the response to Gaussian noise we find that CNNs are still able to identify BBH signals. This provides early evidence that the basis response alone can



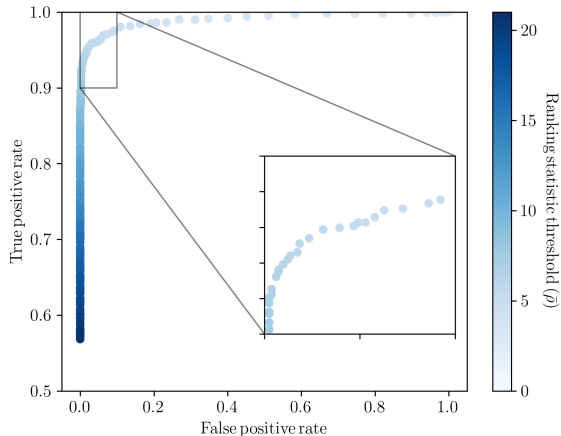


FIG. 5. Receiver operating characteristic (ROC) curve for our toy model as a function of the decision threshold,  $\bar{\rho}$ . For  $\bar{\rho} \geq 8$ , the toy model produces no false positives in our test set of  $\sim 1000$  simulations. The true positive rate, however, indicates that at this threshold approximately  $\sim 10\%$  of astrophysical transients are misclassified.

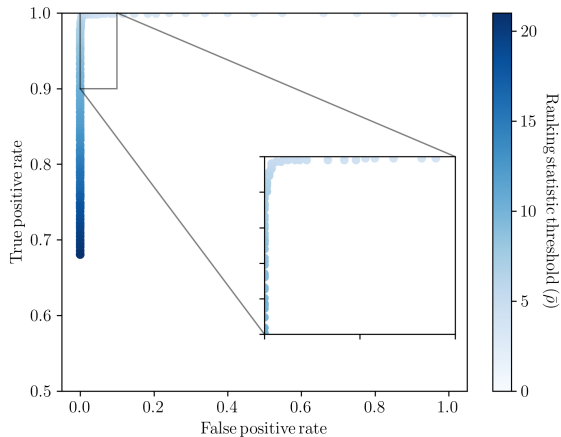


FIG. 6. Receiver operating characteristic (ROC) curve for our  $\mathcal{P}_{\text{glitch}}$  weighted toy model as a function of the decision threshold,  $\bar{\rho}$ . For  $\bar{\rho} \geq 6$ , the updated model produces no false positives. The TPR at this threshold is 100%; at  $\bar{\rho} = 8$ , this only decreases to 99%.

be used for detecting compact binaries, which agrees with previous analytic work [78].

Finally, we note that this method is meant to target transients that occur in times with one operating interferometer, but it is possible to add detectors as an additional channel in our CNN. We leave studies on the performance of this method in multiple interferometer time and its coupling to other noise suppression techniques for future work.

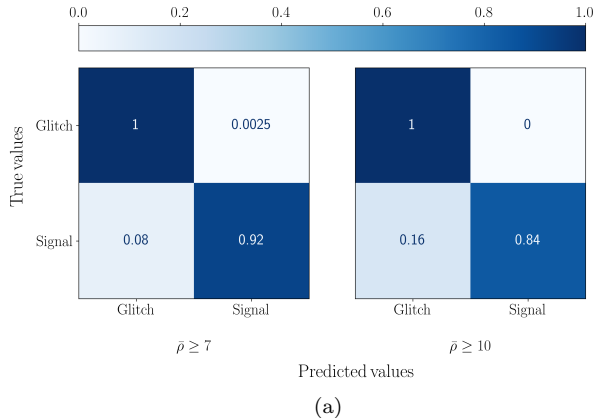


FIG. 7. Confusion matrices for BBH recovery by the toy model pipeline for the glitch-like bank at 2 fiducial detection statistic thresholds. The false positive rates are 0.7% and  $\lesssim 0.1\%$  our low and high thresholds, respectively. The TPR, however, is more tightly coupled to the detection threshold. While 94% of signals are correctly classified at  $\bar{\rho} = 7$ , we find that at a threshold of  $\bar{\rho} = 10$  up 16% of BBHs are missed.

## ACKNOWLEDGMENTS

We gratefully acknowledge informative conversations with Cody Messick. LIGO was constructed by the California Institute of Technology and Massachusetts Institute of Technology with funding from the National Science Foundation and operates under cooperative agreement PHY-1764464. This research has made use of data, software and/or web tools obtained from the Gravitational Wave Open Science Center (<https://www.gwopenscience.org>), a service of LIGO Laboratory, the LIGO Scientific Collaboration and the Virgo Collaboration. Virgo is funded by the French Centre National de Recherche Scientifique (CNRS), the Italian Istituto

Nazionale della Fisica Nucleare (INFN) and the Dutch Nikhef, with contributions by Polish and Hungarian institutes. This material is based upon work supported by NSF's LIGO Laboratory which is a major facility fully funded by the National Science Foundation. The authors are grateful for computational resources provided by the LIGO Laboratory and supported by NSF Grants PHY-0757058 and PHY-0823459. This research has made use of data or software obtained from the Gravitational Wave Open Science Center ([gwosc.org](http://gwosc.org)), a service of LIGO Laboratory, the LIGO Scientific Collaboration, the Virgo Collaboration, and KAGRA. This paper carries LIGO document number LIGO-P2400426. The filtering was performed with the GSTLAL library [27, 70–72], built on the LALSUITE software library [108].

- 
- [1] J. Aasi *et al.* (LIGO Scientific), *Class. Quant. Grav.* **32**, 074001 (2015), arXiv:1411.4547 [gr-qc].
- [2] F. Acernese *et al.* (VIRGO), *Class. Quant. Grav.* **32**, 024001 (2015), arXiv:1408.3978 [gr-qc].
- [3] R. Abbott *et al.* (LIGO Scientific, VIRGO, KAGRA), (2021), arXiv:2111.03606 [gr-qc].
- [4] R. Abbott *et al.* (LIGO Scientific, VIRGO), *Phys. Rev. D* **109**, 022001 (2024), arXiv:2108.01045 [gr-qc].
- [5] R. Abbott *et al.* (LIGO Scientific, Virgo), *Phys. Rev. X* **11**, 021053 (2021), arXiv:2010.14527 [gr-qc].
- [6] B. P. Abbott *et al.* (LIGO Scientific, Virgo), *Phys. Rev. X* **9**, 031040 (2019), arXiv:1811.12907 [astro-ph.HE].
- [7] A. H. Nitz, C. Capano, A. B. Nielsen, S. Reyes, R. White, D. A. Brown, and B. Krishnan, *Astrophys. J.* **872**, 195 (2019), arXiv:1811.01921 [gr-qc].
- [8] R. Magee *et al.*, *Astrophys. J. Lett.* **878**, L17 (2019), arXiv:1901.09884 [gr-qc].
- [9] T. Venumadhav, B. Zackay, J. Roulet, L. Dai, and M. Zaldarriaga, *Phys. Rev. D* **101**, 083030 (2020), arXiv:1904.07214 [astro-ph.HE].
- [10] B. Zackay, L. Dai, T. Venumadhav, J. Roulet, and M. Zaldarriaga, *Phys. Rev. D* **104**, 063030 (2021), arXiv:1910.09528 [astro-ph.HE].
- [11] A. H. Nitz, T. Dent, G. S. Davies, S. Kumar, C. D. Capano, I. Harry, S. Mozzon, L. Nuttall, A. Lundgren, and M. Tápai, *Astrophys. J.* **891**, 123 (2020), arXiv:1910.05331 [astro-ph.HE].
- [12] A. H. Nitz, C. D. Capano, S. Kumar, Y.-F. Wang, S. Kastha, M. Schäfer, R. Dhurkunde, and M. Cabero, *Astrophys. J.* **922**, 76 (2021), arXiv:2105.09151 [astro-ph.HE].
- [13] A. H. Nitz, S. Kumar, Y.-F. Wang, S. Kastha, S. Wu, M. Schäfer, R. Dhurkunde, and C. D. Capano, *Astrophys. J.* **946**, 59 (2023), arXiv:2112.06878 [astro-ph.HE].
- [14] S. Olsen, T. Venumadhav, J. Mushkin, J. Roulet, B. Zackay, and M. Zaldarriaga, *Phys. Rev. D* **106**, 043009 (2022), arXiv:2201.02252 [astro-ph.HE].
- [15] R. Abbott *et al.* (KAGRA, VIRGO, LIGO Scientific), *Phys. Rev. X* **13**, 011048 (2023), arXiv:2111.03634 [astro-ph.HE].
- [16] B. P. Abbott *et al.* (LIGO Scientific, Virgo), *Phys. Rev. Lett.* **123**, 011102 (2019), arXiv:1811.00364 [gr-qc].
- [17] R. Abbott *et al.* (LIGO Scientific, VIRGO, KAGRA), (2021), arXiv:2112.06861 [gr-qc].
- [18] B. P. Abbott *et al.* (LIGO Scientific, Virgo), *Phys. Rev. Lett.* **121**, 161101 (2018), arXiv:1805.11581 [gr-qc].
- [19] B. P. Abbott *et al.* (LIGO Scientific, Virgo), *Astrophys. J. Lett.* **892**, L3 (2020), arXiv:2001.01761 [astro-ph.HE].
- [20] R. Abbott *et al.* (LIGO Scientific, Virgo), *Astrophys. J. Lett.* **896**, L44 (2020), arXiv:2006.12611 [astro-ph.HE].
- [21] R. Abbott *et al.* (LIGO Scientific, Virgo), *Phys. Rev. Lett.* **125**, 101102 (2020), arXiv:2009.01075 [gr-qc].
- [22] A. G. Abac *et al.* (LIGO Scientific, VIRGO, KAGRA), (2024), arXiv:2404.04248 [astro-ph.HE].
- [23] M. Zevin, S. S. Bavera, C. P. L. Berry, V. Kalogera, T. Fragos, P. Marchant, C. L. Rodriguez, F. Antonini, D. E. Holz, and C. Pankow, *Astrophys. J.* **910**, 152 (2021), arXiv:2011.10057 [astro-ph.HE].
- [24] C. Messenger and J. Veitch, *New J. Phys.* **15**, 053027 (2013), arXiv:1206.3461 [astro-ph.IM].
- [25] R. Magee, M. Isi, E. Payne, K. Chatziioannou, W. M. Farr, G. Pratten, and S. Vitale, *Phys. Rev. D* **109**, 023014 (2024), arXiv:2311.03656 [gr-qc].
- [26] B. P. Abbott *et al.* (LIGO Scientific, Virgo), *Class. Quant. Grav.* **35**, 065010 (2018), arXiv:1710.02185 [gr-qc].
- [27] L. Tsukada *et al.*, *Phys. Rev. D* **108**, 043004 (2023), arXiv:2305.06286 [astro-ph.IM].
- [28] F. Aubin *et al.*, *Class. Quant. Grav.* **38**, 095004 (2021), arXiv:2012.11512 [gr-qc].
- [29] A. H. Nitz, T. Dal Canton, D. Davis, and S. Reyes, *Phys. Rev. D* **98**, 024050 (2018), arXiv:1805.11174 [gr-qc].
- [30] E. Cuoco *et al.*, *Mach. Learn. Sci. Tech.* **2**, 011002 (2021), arXiv:2005.03745 [astro-ph.HE].
- [31] N. Stergioulas (2024) arXiv:2401.07406 [gr-qc].
- [32] D. George and E. A. Huerta, *Phys. Lett. B* **778**, 64 (2018), arXiv:1711.03121 [gr-qc].
- [33] H. Gabbard, M. Williams, F. Hayes, and C. Messenger, *Phys. Rev. Lett.* **120**, 141103 (2018), arXiv:1712.06041 [astro-ph.IM].
- [34] P. Nousi, A. E. Koloniari, N. Passalis, P. Iosif, N. Stergioulas, and A. Tefas, *Phys. Rev. D* **108**, 024022 (2023), arXiv:2211.01520 [gr-qc].
- [35] E. Marx *et al.*, (2024), arXiv:2403.18661 [gr-qc].

- [36] R. Alfaidi and C. Messenger, (2024), arXiv:2402.04589 [gr-qc].
- [37] M. B. Schäfer *et al.*, Phys. Rev. D **107**, 023021 (2023), arXiv:2209.11146 [astro-ph.IM].
- [38] T. Mishra *et al.*, Phys. Rev. D **105**, 083018 (2022), arXiv:2201.01495 [gr-qc].
- [39] P. G. Krastev, Phys. Lett. B **803**, 135330 (2020), arXiv:1908.03151 [astro-ph.IM].
- [40] M. B. Schäfer, F. Ohme, and A. H. Nitz, Phys. Rev. D **102**, 063015 (2020), arXiv:2006.01509 [astro-ph.HE].
- [41] W. Wei and E. A. Huerta, Phys. Lett. B **816**, 136185 (2021), arXiv:2010.09751 [gr-qc].
- [42] G. Baltus, J. Janquart, M. Lopez, A. Reza, S. Caudill, and J.-R. Cudell, Phys. Rev. D **103**, 102003 (2021), arXiv:2104.00594 [gr-qc].
- [43] H. Yu, R. X. Adhikari, R. Magee, S. Sachdev, and Y. Chen, Phys. Rev. D **104**, 062004 (2021), arXiv:2104.09438 [gr-qc].
- [44] G. Baltus, J. Janquart, M. Lopez, H. Narola, and J.-R. Cudell, Phys. Rev. D **106**, 042002 (2022), arXiv:2205.04750 [gr-qc].
- [45] P. Astone, P. Cerdá-Durán, I. Di Palma, M. Drago, F. Muciaccia, C. Palomba, and F. Ricci, Phys. Rev. D **98**, 122002 (2018), arXiv:1812.05363 [astro-ph.IM].
- [46] J. M. Antelis, M. Cavaglia, T. Hansen, M. D. Morales, C. Moreno, S. Mukherjee, M. J. Szczepańczyk, and M. Zanolin, Phys. Rev. D **105**, 084054 (2022), arXiv:2111.07219 [gr-qc].
- [47] M. López Portilla, I. D. Palma, M. Drago, P. Cerdá-Durán, and F. Ricci, Phys. Rev. D **103**, 063011 (2021), arXiv:2011.13733 [astro-ph.IM].
- [48] H. Gabbard, C. Messenger, I. S. Heng, F. Tonolini, and R. Murray-Smith, Nature Phys. **18**, 112 (2022), arXiv:1909.06296 [astro-ph.IM].
- [49] M. Dax, S. R. Green, J. Gair, J. H. Macke, A. Buonanno, and B. Schölkopf, Phys. Rev. Lett. **127**, 241103 (2021), arXiv:2106.12594 [gr-qc].
- [50] C. Chatterjee, L. Wen, D. Beveridge, F. Diakogiannis, and K. Vinsen, (2022), arXiv:2207.14522 [gr-qc].
- [51] C. Chatterjee and L. Wen, (2022), arXiv:2301.03558 [astro-ph.HE].
- [52] M. Dax, S. R. Green, J. Gair, M. Pürrer, J. Wildberger, J. H. Macke, A. Buonanno, and B. Schölkopf, Phys. Rev. Lett. **130**, 171403 (2023), arXiv:2210.05686 [gr-qc].
- [53] K. W. K. Wong, M. Isi, and T. D. P. Edwards, (2023), arXiv:2302.05333 [astro-ph.IM].
- [54] S. Schmidt, M. Breschi, R. Gamba, G. Pagano, P. Retegno, G. Riemenschneider, S. Bernuzzi, A. Nagar, and W. Del Pozzo, Phys. Rev. D **103**, 043020 (2021), arXiv:2011.01958 [gr-qc].
- [55] A. J. K. Chua, C. R. Galley, and M. Vallisneri, Phys. Rev. Lett. **122**, 211101 (2019), arXiv:1811.05491 [astro-ph.IM].
- [56] S. Khan and R. Green, Phys. Rev. D **103**, 064015 (2021), arXiv:2008.12932 [gr-qc].
- [57] J. Tissino, G. Carullo, M. Breschi, R. Gamba, S. Schmidt, and S. Bernuzzi, Phys. Rev. D **107**, 084037 (2023), arXiv:2210.15684 [gr-qc].
- [58] L. M. Thomas, G. Pratten, and P. Schmidt, Phys. Rev. D **106**, 104029 (2022), arXiv:2205.14066 [gr-qc].
- [59] R. Magee, R. George, A. Li, and R. Sharma, (2024), arXiv:2408.02470 [astro-ph.IM].
- [60] G. Vajente, Y. Huang, M. Isi, J. C. Driggers, J. S. Kissel, M. J. Szczepańczyk, and S. Vitale, Phys. Rev. D **101**, 042003 (2020), arXiv:1911.09083 [gr-qc].
- [61] R. Essick, P. Godwin, C. Hanna, L. Blackburn, and E. Katsavounidis, (2020), arXiv:2005.12761 [astro-ph.IM].
- [62] M. Saleem *et al.*, (2023), arXiv:2306.11366 [gr-qc].
- [63] M. Zevin *et al.*, Class. Quant. Grav. **34**, 064003 (2017), arXiv:1611.04596 [gr-qc].
- [64] J. Glanzer *et al.*, Class. Quant. Grav. **40**, 065004 (2023), arXiv:2208.12849 [gr-qc].
- [65] J. D. Merritt, B. Farr, *et al.*, Phys. Rev. D **104**, 11 (2021), arXiv:2108.12044 [gr-qc].
- [66] M. Lopez, V. Boudart, K. Buijsman, A. Reza, and S. Caudill, Phys. Rev. D **106**, 023027 (2022), arXiv:2203.06494 [astro-ph.IM].
- [67] M. Lopez, V. Boudart, S. Schmidt, and S. Caudill, arXiv e-prints, arXiv:2205.09204 (2022), arXiv:2205.09204 [astro-ph.IM].
- [68] M. Cabero *et al.*, Class. Quant. Grav. **36**, 15 (2019), arXiv:1901.05093 [physics.ins-det].
- [69] D. Davis, L. V. White, and P. R. Saulson, Class. Quant. Grav. **37**, 145001 (2020), arXiv:2002.09429 [gr-qc].
- [70] C. Messick *et al.*, Phys. Rev. D **95**, 042001 (2017), arXiv:1604.04324 [astro-ph.IM].
- [71] S. Sachdev *et al.*, (2019), arXiv:1901.08580 [gr-qc].
- [72] K. Cannon, S. Caudill, C. Chan, B. Cousins, J. D. E. Creighton, B. Ewing, H. Fong, P. Godwin, C. Hanna, S. Hooper, R. Huxford, R. Magee, D. Meacher, C. Messick, S. Morisaki, D. Mukherjee, H. Ohta, A. Pace, S. Privitera, I. de Ruiter, S. Sachdev, L. Singer, D. Singh, R. Tapia, L. Tsukada, D. Tsuna, T. Tsutsui, K. Ueno, A. Viets, L. Wade, and M. Wade, SoftwareX **14**, 100680 (2021), arXiv:2010.05082 [astro-ph.IM].
- [73] Y. LeCun, Y. Bengio, and G. Hinton, Nature **521**, 436 (2015).
- [74] J. Schmidhuber, arXiv e-prints, arXiv:1404.7828 (2014), arXiv:1404.7828 [cs.NE].
- [75] K. Cannon, A. Chapman, C. Hanna, D. Keppel, A. C. Searle, and A. J. Weinstein, Phys. Rev. D **82**, 044025 (2010), arXiv:1005.0012 [gr-qc].
- [76] K. Cannon, C. Hanna, and D. Keppel, Phys. Rev. D **84**, 084003 (2011), arXiv:1101.4939 [gr-qc].
- [77] K. Cannon, C. Hanna, and D. Keppel, Phys. Rev. D **85**, 081504 (2012), arXiv:1108.5618 [gr-qc].
- [78] K. Cannon, C. Hanna, D. Keppel, and A. C. Searle, Phys. Rev. D **83**, 084053 (2011), arXiv:1101.0584 [physics.data-an].
- [79] S. Soni *et al.* (LIGO), Class. Quant. Grav. **38**, 025016 (2020), arXiv:2007.14876 [astro-ph.IM].
- [80] J. Powell, L. Sun, K. Gereb, P. D. Lasky, and M. Dollmann, Class. Quant. Grav. **40**, 035006 (2023), arXiv:2207.00207 [astro-ph.IM].
- [81] I. J. Goodfellow, J. Pouget-Abadie, M. Mirza, B. Xu, D. Warde-Farley, S. Ozair, A. Courville, and Y. Bengio, arXiv e-prints, arXiv:1406.2661 (2014), arXiv:1406.2661 [stat.ML].
- [82] T. Accadia *et al.*, Class. Quant. Grav. **27**, 194011 (2010).
- [83] S. Soni *et al.*, (2024), arXiv:2409.02831 [astro-ph.IM].
- [84] R. Udall and D. Davis, Appl. Phys. Lett. **122**, 094103 (2023), arXiv:2211.15867 [astro-ph.IM].
- [85] B. J. Owen and B. S. Sathyaprakash, Phys. Rev. D **60**, 022002 (1999), arXiv:gr-qc/9808076.
- [86] I. W. Harry, B. Allen, and B. S. Sathyaprakash, Phys.

- Rev. D **80**, 104014 (2009), arXiv:0908.2090 [gr-qc].
- [87] S. Privitera, S. R. P. Mohapatra, P. Ajith, K. Cannon, N. Fotopoulos, M. A. Frei, C. Hanna, A. J. Weinstein, and J. T. Whelan, Phys. Rev. D **89**, 024003 (2014), arXiv:1310.5633 [gr-qc].
- [88] S. Khan, S. Husa, M. Hannam, F. Ohme, M. Pürrer, X. Jiménez Forteza, and A. Bohé, Phys. Rev. D **93**, 044007 (2016), arXiv:1508.07253 [gr-qc].
- [89] S. Sakon *et al.*, (2022), arXiv:2211.16674 [gr-qc].
- [90] A. Bohé *et al.*, Phys. Rev. D **95**, 044028 (2017), arXiv:1611.03703 [gr-qc].
- [91] K. Cannon *et al.*, Astrophys. J. **748**, 136 (2012), arXiv:1107.2665 [astro-ph.IM].
- [92] S. Sachdev *et al.*, Astrophys. J. Lett. **905**, L25 (2020), arXiv:2008.04288 [astro-ph.HE].
- [93] J. Abadie *et al.* (LIGO Scientific, VIRGO), Phys. Rev. D **85**, 082002 (2012), arXiv:1111.7314 [gr-qc].
- [94] S. Babak, R. Biswas, P. Brady, D. Brown, K. Cannon, *et al.*, Phys. Rev. D **87**, 024033 (2013), arXiv:1208.3491 [gr-qc].
- [95] B. Xu, N. Wang, T. Chen, and M. Li, arXiv e-prints, arXiv:1505.00853 (2015), arXiv:1505.00853 [cs.LG].
- [96] R. Macas, J. Pooley, L. K. Nuttall, D. Davis, M. J. Dyer, Y. Lecoecueche, J. D. Lyman, J. McIver, and K. Rink, Phys. Rev. D **105**, 103021 (2022), arXiv:2202.00344 [astro-ph.HE].
- [97] D. P. Kingma and J. Ba (2014) arXiv:1412.6980 [cs.LG].
- [98] C. J. Van Rijsbergen, “Information retrieval. 2nd. newton, ma,” (1979).
- [99] W. J. Youden, Cancer **3**, 32 (1950), [https://doi.org/10.1002/1097-0142\(1950\)3:1;32::AID-CNCR2820030106;3.0.CO;2-3](https://doi.org/10.1002/1097-0142(1950)3:1;32::AID-CNCR2820030106;3.0.CO;2-3).
- [100] B. Matthews, Biochimica et Biophysica Acta (BBA) - Protein Structure **405**, 442 (1975).
- [101] J. Cohen, Educational and Psychological Measurement **20**, 37 (1960), <https://doi.org/10.1177/001316446002000104>.
- [102] S. V. Stehman, Remote Sensing of Environment **62**, 77 (1997).
- [103] S. E. Woosley, Astrophys. J. **836**, 244 (2017), arXiv:1608.08939 [astro-ph.HE].
- [104] K. Belczynski *et al.*, Astron. Astrophys. **594**, A97 (2016), arXiv:1607.03116 [astro-ph.HE].
- [105] N. Giacobbo, M. Mapelli, and M. Spera, Mon. Not. Roy. Astron. Soc. **474**, 2959 (2018), arXiv:1711.03556 [astro-ph.SR].
- [106] M. Spera and M. Mapelli, Mon. Not. Roy. Astron. Soc. **470**, 4739 (2017), arXiv:1706.06109 [astro-ph.SR].
- [107] R. Abbott *et al.* (LIGO Scientific, Virgo), Astrophys. J. Lett. **900**, L13 (2020), arXiv:2009.01190 [astro-ph.HE].
- [108] LIGO Scientific Collaboration and Virgo Collaboration, “LALSuite software,” (2018).